Fluctuations in the composition of nuclear pasta in symmetric nuclear matter at finite temperature

Celso C. Barros, Jr.,[1] Débora P. Menezes,[1] and Francesca Gulminelli[2]
[1]*Depto de Física, CFM, Universidade Federal de Santa Catarina Florianópolis, SC, CP. 476, CEP 88.040, 900, Brazil*
[2]*CNRS and ENSICAEN, UMR6534, LPC, 14050 Caen cédex, France*

(Received 6 November 2019; revised manuscript received 5 February 2020; accepted 19 February 2020; published 30 March 2020)

The equilibrium distributions of the different pasta geometries and their linear sizes are calculated from the mean field Gibbs energy functional in symmetric nuclear matter at finite temperature. The average sizes and shapes coincide approximately with the ones predicted by a standard pasta calculation in the coexisting phase approximation, but fluctuations are additionally calculated and seen to increase with temperature and baryonic density. The different pasta shapes are shown to coexist in a wide domain of density and temperature, in qualitative agreement with the findings of large scale molecular dynamics simulations, but with a much less expensive computational cost.

DOI: 10.1103/PhysRevC.101.035211

I. INTRODUCTION

Exotic nonspherical shapes of nuclear matter, the so-called pasta phases, are possible because of a competition between short range nuclear attraction and long range Coulomb repulsion, leading to the phenomenon of Coulomb frustration, well known in statistical mechanics [1]. Such complex phases are expected in the inner crust of neutron stars (NS), as well as in core-collapse supernova cores [2–6].

Even if their existence is limited to a very narrow range of densities, their electrical and thermal conductivity are believed to be very important for the thermal [7,8] and magnetic evolution of neutron stars [9,10], and their elastic properties give some information on the quasiperiodic oscillations (QPOs) observed in some soft-gamma ray repeaters (SGR) [11] and on magnetar giant flares [12]. Moreover, in supernova matter, the presence of density inhomogeneities contributes in an important way to neutrino opacity [10,13–15]. In particular, it was suggested that pasta can slow neutrino diffusion in protoneutron stars and greatly increase the neutrino signal at late times after core collapse [16].

Most calculations of nuclear pasta assume a crystalline structure in the so-called single nucleus approximation (SNA): different pasta geometries and sizes are associated to different temperatures, densities, and proton fractions, but at a given thermodynamic condition matter is described by the spatial repetition of identical Wigner-Seitz cells. This is a poor approximation because at finite temperature different configurations can coexist at thermal equilibrium, and a rich phenomenology corresponding to multiple domains and defects is expected [17]. These fluctuations of composition are believed to be particularly important in the case of pasta, because of the very small energy barriers separating different geometries [18]. In the calculations of crustal heating and cooling, these defects are modelled by an external impurity factor, which is essentially a free parameter [19].

The importance of fluctuations is confirmed by the realistic, and numerically very expensive, molecular dynamics simulations of nuclear pasta that go beyond the SNA: hundreds of thousands of particles are needed to avoid deformations due to boundary conditions and finite size effects [20,21]. These calculations treat nucleons as purely classical particles. Self-consistent mean-field approximations with realistic effective interactions have also been performed [22–24], but no more than some thousand nucleons can be simulated even if massive parallel computing is employed [24]. Shell and finite size effects were also investigated with the help of Skyrme-Hartree-Fock equations solved on a three-dimensional (3D) Cartesian grid and some impressive structures were obtained. These effects were shown to be minimized only for very large number of nucleons, of at least $A = 2000$ [25]. In these microscopic studies, it was observed that complex geometries different from the standard spheres, slabs and rods can be obtained, though at a very expensive computational cost. However, it is not clear if those triple periodic minimal surface (TPMS) pasta configurations [26] will survive at finite temperature, which is the object of the present study. For this reason, we stick to the standard pasta geometries in the following.

In a recent paper [27], a perturbative method was introduced, allowing to calculate the full nuclear distribution associated to a given equation of state (EoS) of stellar matter based on the single-nucleus Wigner-Seitz approximation, with a numerical effort comparable to the one needed for a simple SNA. In this approach, the different configurations are weighted according to their Gibbs energy, which is consistently calculated from the EoS. The only hypothesis needed is that the corrections to the chemical potentials calculated in the SNA can be treated perturbatively, and neglected at first order. This hypothesis can be considered as safe in the high temperature domain investigated in the present work, as it was recognized already in the 1980s [28]. This technique

was applied in Ref. [27] to evaluate the nuclear distribution during core collapse, based on a nonrelativistic equation of state. In this paper, we use the same formalism but we apply it to a relativistic mean-field functional. Furthermore, we use it for the first time to compute the distributions in the pasta regime, and show that at moderate temperature the different pasta geometries can coexist with comparable probabilities in a large range of densities, at very low computational cost.

The plan of the paper is as follows. In Sec. II the theoretical formalism is presented. After a short summary of the main equations for a relativistic mean-field treatment of finite temperature homogeneous matter in Sec. II A. In Sec. II B we show how the free energy for the different pasta geometries is computed and in Sec. II C the statistical formalism allowing to calculate the pasta distributions and the multicomponent (or NSE) formalism used for this study is recalled. For this exploratory study, we limit ourselves to symmetric matter. This has not a direct application for astrophysical purposes, but allows describing the main features of the pasta distributions as a function of density and temperature. The extension to asymmetric matter is in progress. The results are presented in Sec. III, and Sec. IV contains conclusions and outlooks.

II. FORMALISM

A. Finite temperature relativistic mean field

We consider a neutral system of electrons, protons and neutrons with masses given respectively by $m_e = 0.511$ MeV and $M = 939$ MeV and their corresponding antiparticles, interacting in the mean-field approximation of static fields with and through an isoscalar-scalar field ϕ_0, an isoscalar-vector field V_0, and an isovector-vector field $\mathbf{b}_0$. The parameters of the models are the meson masses m_s, m_v, m_ρ, the linear coupling parameters g_s, g_v, g_ρ of the mesons to the nucleons, and the nonlinear scalar couplings κ, λ, for which we use the NL3 [29] parameter set.

The bulk nuclear matter properties of the NL3 model are the binding energy $B/A = 16.3$ MeV, the compressibility $K = 272$ MeV, the symmetry energy $E_{\rm sym} = 32.4$ MeV, the effective mass $M^*/M = 0.60$, and the slope of the symmetry energy $L = 93.9$ MeV, all calculated at the saturation density of the model $\rho_0 = 0.148\,\mathrm{fm}^{-3}$. It is well known that this parameter set is not one of the most realistic RMF models [30]. Nevertheless, the unphysical characteristics of NL3 mainly appear at densities above nuclear saturation and for asymmetric matter, situations which are not explored in the present work. Conversely, a reliable calculation of the surface tension coefficient was obtained for NL3 within the self-consistent microscopic Thomas-Fermi approximation [31]. As it will be clear in the following, a consistent treatment of surface and bulk is crucial to obtain realistic results in a pasta calculation, and this is the reason why this parametrization was often employed in previous works that use the same formalism [13,31–33].

In future calculations, realistic proton fractions for astrophysical applications will be considered, and the parametrization will be reviewed.

The following equations of motion for the fields are obtained and solved self-consistently [32,33,35]:

$$\begin{aligned} m_s^2\phi_0 + \frac{\kappa}{2}\phi_0^2 + \frac{\lambda}{6}\phi_0^3 &= g_s\rho_s, \\ m_v^2 V_0 = g_v\rho_B \;;\; m_\rho^2 b_0 &= \frac{g_\rho}{2}\rho_3. \end{aligned} \tag{1}$$

They depend on the the equilibrium densities $\rho_B = \rho_p + \rho_n$, $\rho_3 = \rho_p - \rho_n$, where ρ_p and ρ_n are the proton and neutron densities, as well as on the associated scalar densities $\rho_s = \rho_{sp} + \rho_{sn}$ and $\rho_{s3} = \rho_{sp} - \rho_{sn}$. The proton/neutron densities are given by

$$\rho_i = \frac{1}{\pi^2}\int_0^\infty dp p^2 (f_{i+} - f_{i-}),\;\; i = p, n \tag{2}$$

and the corresponding scalar density by

$$\rho_{s_i} = \frac{1}{\pi^2}\int_0^\infty dp p^2 \frac{M_i^*}{\sqrt{p^2 + M_i^{*2}}}(f_{i+} + f_{i-}) \tag{3}$$

with the distribution functions given by

$$f_{i\pm} = \frac{1}{1 + \exp[(\epsilon_i^*(\mathbf{p}) \mp \nu_i)/T]}\,, \tag{4}$$

where $\epsilon_i^* = \sqrt{\mathbf{p}^2 + M_i^{*2}}$,

$$M_i^* = M - g_s\,\phi_0, \tag{5}$$

and the effective chemical potentials are

$$\nu_i = \mu_i - g_v V_0 - \frac{g_\rho}{2}\,\tau_{3i}\,b_0, \tag{6}$$

$\tau_{3i} = \pm 1$ being the isospin projection for the protons and neutrons, respectively. The baryonic free energy density is defined as

$$\mathcal{F} = \mathcal{E} - T\mathcal{S}, \tag{7}$$

where the energy density is given by

$$\begin{aligned} \mathcal{E} = {} & \frac{1}{\pi^2}\sum_{i=n,p}\int_0^\infty dp p^2 \epsilon_i^*(f_{i+} + f_{i-}) \\ & + \frac{m_v^2}{2}V_0^2 + \frac{m_\rho^2}{2}b_0^2 + \frac{m_s^2}{2}\phi_0^2 + \frac{k}{6}\phi_0^3 + \frac{\lambda}{24}\phi_0^4, \end{aligned} \tag{8}$$

and the entropy density reads

$$\mathcal{S} = \frac{1}{T}(\mathcal{E} + P - \mu_p\rho_p - \mu_n\rho_n), \tag{9}$$

as a function of the baryonic pressure

$$\begin{aligned} P = {} & \frac{1}{3\pi^2}\sum_{i=p,n}\int_0^\infty dp \frac{p^4}{\epsilon_i^*}(f_{i+} + f_{i-}) \\ & + \frac{m_v^2}{2}V_0^2 + \frac{\xi g_v^4}{24}V_0^4 + \frac{m_\rho^2}{2}b_0^2 - \frac{m_s^2}{2}\phi_0^2 \\ & - \frac{\kappa}{6}\phi_0^3 - \frac{\lambda}{24}\phi_0^4. \end{aligned} \tag{10}$$

We always consider neutral matter and therefore the electron density is equal to the density of the protons. The leptonic

thermodynamic quantities are given by standard relativistic free Fermi gas, and explicit expressions can be found in Refs. [32,33].

B. Nuclear pasta within the coexisting phases method

As in [6,33], for a given total density ρ_B and proton fraction $Y_p = \rho_p/\rho_B = \rho_e/\rho_B$ (with ρ_e the net electron density), the average characteristics of the pasta structures are built with different geometrical forms in a background nucleon and electron gas. This is achieved within the so-called coexisting phase approximations (CPA). The cluster and the gas are distributed in two homogeneous components at different densities ρ^I and ρ^{II} each satisfying the self-consistent equations (1) for the scalar fields. The equilibrium between the two components is obtained imposing equality of pressure and chemical potentials:

$$P^I\left(\nu_p^I, \nu_n^I, M_n^{*I}, M_p^{*I}\right) = P^{II}\left(\nu_p^{II}, \nu_n^{II}, M_n^{*II}, M_p^{*II}\right),$$
$$\mu_i^I = \mu_i^{II}, \quad i = p, n. \tag{11}$$

Finally particle number conservation defines the volume fraction $f^I \equiv f$ of the dense "phase":

$$f = \frac{\rho_B - \rho^{II}}{\rho^I - \rho^{II}} \tag{12}$$

with ρ_B and $\rho_p = \rho_e$ the total baryonic and proton density, the latter being also equal to the net electron density, which is considered as homogeneous over the Wigner-Seitz cell, i.e., $\rho_e^I = \rho_e^{II}$. The solution of the above equations allows estimating, for a given thermodynamic condition (T, ρ_B, Y_p), the mass and volume fraction associated to clusterized matter, but not the cluster shape nor its linear dimension. These latter can be variationally determined introducing finite size effects, namely the interplay between Coulomb and surface energy. The total baryonic energy density of the cell is given by

$$\mathcal{E}_D = f\mathcal{E}^I + (1-f)\mathcal{E}^{II} + \mathcal{E}_{\mathrm{surf},D} + \mathcal{E}_{\mathrm{Coul},D}, \tag{13}$$

where $\mathcal{E}^{I(II)}$ is the baryonic energy density of homogeneous matter at the baryonic density $\rho^{I(II)}$ given by Eq. (8). This term only depends on the densities $\rho^{I(II)}$, $\rho_p^{I(II)}$, while the surface and Coulomb term additionally depend on the assumed geometry ($D = 1, 2, 3$). By minimizing the sum $\mathcal{E}_{\mathrm{surf},D} + \mathcal{E}_{\mathrm{Coul},D}$ with respect to the size of the droplet/bubble, rod/tube, or slab we get the virial condition [6] $\mathcal{E}_{\mathrm{surf},D} = 2\mathcal{E}_{\mathrm{Coul},D}$, and

$$\mathcal{E}_{\mathrm{Coul},D} = \frac{2\beta}{4^{2/3}}(e^2\pi\Phi_D)^{1/3}\left(\sigma D\left(\rho_p^I - \rho_p^{II}\right)\right)^{2/3}, \tag{14}$$

where $\beta = f$ for droplets and $\beta = 1 - f$ for bubbles, σ is the surface energy coefficient, D is the dimension of the system. For droplets, rods, and slabs,

$$\Phi_D = \begin{cases} \left(\frac{2-Df^{1-2/D}}{D-2} + f\right)\frac{1}{D+2}, & D = 1, 3; \\ \frac{f-1-\ln(f)}{D+2}, & D = 2. \end{cases} \tag{15}$$

The results of the CPA can be realistic if the surface tension coefficient σ is microscopically calculated [31–33]. We use the functional form given in [31] for the the surface tension coefficient, which was fitted from a full variation of the local density profile in the Thomas-Fermi approximation. Each structure is considered to be in the center of a charge neutral Wigner-Seitz cell constituted by neutrons, protons and leptons (electrons and positrons) [34]. This average Wigner-Seitz cell is a sphere/cylinder/slab whose volume is the same as the unit BCC cell. The linear size of the droplet (rod, slab) and of the Wigner-Seitz cell are, respectively, given by

$$R_D = \left(\frac{\sigma D}{4\pi e^2\left(\rho_p^I - \rho_p^{II}\right)^2\Phi_D}\right)^{1/3}, \quad R_W = \frac{R_D}{f^{1/D}}. \tag{16}$$

In the SNA approximation, the equilibrium configuration in a given thermodynamic condition is characterized by the repetition in space of a unique geometry, which will be referred to as the pasta solution. This solution is determined by comparing the total free energy per particle as obtained in the different geometries [2–6,31–33,35]. As a general trend, the droplet shape prevails at the lowest densities, and is replaced successively by rods, slabs, and bubbles as density increases. The location of the transition between the different geometries depends on the temperature, the proton fraction, and, to a smaller degree, on the nuclear model [36].

An example is given in Fig. 1 at two different temperatures ($T = 1$ and 5.5 MeV), from where one can see the actual values of the free energy per particle in the different geometries and densities. We can see that the free energy barrier between the different configurations is extremely low in a wide range of densities, and a qualitatively similar behavior is observed in the whole sub-saturation density domain. This is a generic result that was observed by many authors [2,3,5,6] with different models. It means that we can expect a strong superposition of different shapes in a complete statistical calculation at finite temperature, as it is indeed observed in large scale molecular dynamics simulations [17,21–24].

The statistical weight of these different configurations is worked out in the next section.

C. Distribution of pasta structures

In a complete statistical mechanics treatment of finite temperature matter, the total free energy should be minimized with respect to the probabilities of the different microstates, and in the absence of long range correlations a statistical distribution of Wigner-Seitz cells is obtained [27,37]. Working in the grand-canonical ensemble, the different cells share the same intensive parameters, namely, the chemical potentials $\mu_n = \mu_n^{II}$, $\mu_p = \mu_p^{II}$ as well as the pressure $P = P^{II}$. As a consequence, the characteristics of the nucleon gas (phase II) are not modified with respect to the CPA treatment. Conversely, the density, proton fraction and geometry can fluctuate from one cell to another.

We follow the derivation of Refs. [27,37,38], but we adapt it to the RMF model and extend it to the case of multiple free energy minima due to the different geometries, which enables multimodal probability distributions.

Since the SNA is known to reproduce very accurately the average thermodynamic properties, we make the approximation that the relation between chemical potential μ_n, μ_p and total baryonic and total density ρ_B, ρ_p can be obtained in the SNA, that is from the solution of the equilibrium Gibbs

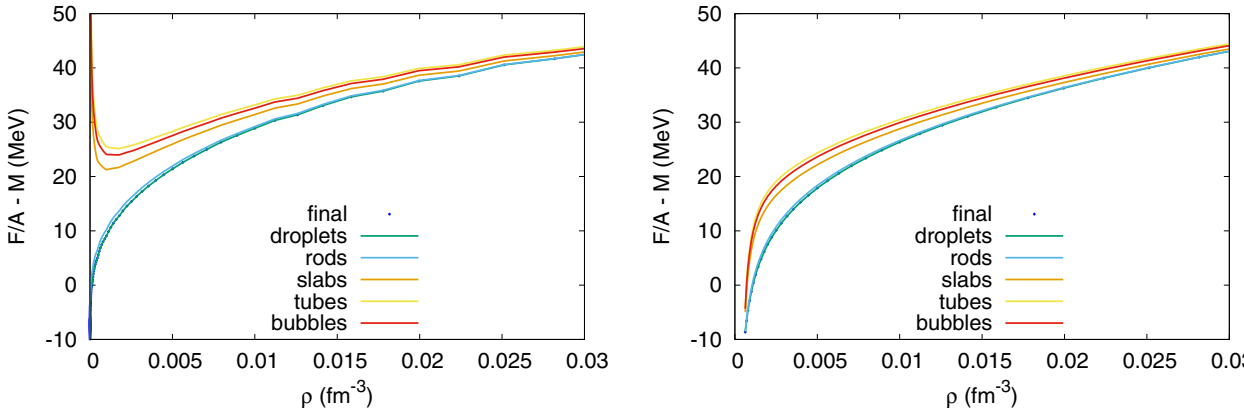

FIG. 1. Free energy per nucleon as a function of the density for $Y_p = 0.5$ and $T = 1$ (left figure) and 5.5 MeV (right figure) for different geometries. The final (preferential) configuration curve coincides with the droplets at the bottom and the subsequent curves (from bottom to top) represent rods, slabs, bubbles, and tubes.

equations of the CPA. The mean field equations require that each pasta configuration corresponding to a given density ρ^N leads to corresponding fluctuating meson fields. The free energy density is still given by Eq. (7), but all the quantities are calculated at a density $\rho = \rho^N$. For a given density value ρ^N, within the volume corresponding to the spherical cell $V_W^N = 4\pi (R_3^N)^3/3 f^N$, the number of particles of the cluster does not depend on the geometry and is given by

$$A^N = \frac{4}{3}\pi \rho^N \left(R_3^N\right)^3 , \tag{17}$$

where R_3^N is given by

$$R_3^N = \left(\frac{3\sigma}{4\pi e^2 \left(\rho_p^N - \rho_p^{II}\right)^2 \Phi_3} \right)^{1/3} . \tag{18}$$

Analogous expressions hold for the proton and neutron number Z^N, N^N of the cluster. For the other geometries, the same volume is fixed in our calculations, in which the number of particles is computed.

To obtain the probability $P_D(A^N)$ of finding a pasta structure with A^N particles per unit cell, and dimension D, we describe the macroscopic system as a collection of independent Wigner-Seitz cells, each one characterized by the same nucleon gas of density ρ^{II}, but different volume fractions f^N and cluster densities ρ^N, leading to different cluster masses $A^N = \rho^N V^N$. The chemical equilibrium is no longer realized at the level of the single cell, but only at the level of the multi-component distribution. Mass and charge conservation now read

$$\rho_B = \sum_{N,D} P_D(A^N)[f^N \rho^N + (1 - f^N)\rho^{II}], \tag{19}$$

$$\rho_p = \sum_{N,D} P_D(A^N)\left[f^N \rho_p^N + (1 - f^N)\rho_p^{II}\right] , \tag{20}$$

where the sum runs over cluster species N and dimensions D. Charge neutrality in principle imposes $\rho_p = \rho_e$ only for the global system, but in fact charge neutrality is also realized at the level of the single Wigner-Seitz cell because of the homogeneity of the electron and proton gas, $\rho_e = \rho_p^N = Y_p^N \rho_B^N$.

The density of clusters corresponding to the fluctuation ρ_N and the geometry D ($n_D(A^N)$) is linked to the probability P^N by

$$n_D(A^N) = P_D(A^N)/V_W \; ; \; V_W = \sum_N V_W^N P_D(A^N), \tag{21}$$

where, as already mentioned, the volume cell does not depend on the geometry, and the average cell volume V_W is taken from the pasta calculation. In the case of the traditional pasta calculation (or SNA approximation), we would have $n^N = 1/V_W$ for $\rho^N = \rho^I$, and zero otherwise. The free energy density of the multicomponent plasma for the ensemble of occupations $\{n_D(A^N)\}$ can be written as

$$\begin{aligned} \mathcal{F} &= \sum_{N,D} n_D(A^N)\left[f^N\left(\mathcal{F}^N + \mathcal{E}^N_{\mathrm{surf},D} + \mathcal{E}^N_{\mathrm{Coul},D}\right)\right]V_W^N \\ &\quad + \sum_{N,D} n_D(A^N)[(1 - f^N)\mathcal{F}^{II}]V_W^N \\ &= \mathcal{F}^{II} + \sum_{N,D} n_D(A^N) F_D(A^N), \end{aligned} \tag{22}$$

where the contribution of the dilute part can be separated from the rest if an in-medium free energy is defined as

$$F_D(A^N) = \frac{A^N}{\rho^N}\left(\mathcal{F}^N + \mathcal{E}^N_{\mathrm{surf},D} + \mathcal{E}^N_{\mathrm{Coul},D} - \mathcal{F}^{II}\right), \tag{23}$$

or also

$$\begin{aligned} F_D(A^N) &= \frac{\mathcal{E}_D(\rho^N) - \mathcal{E}(\rho^{II})}{\rho^N} A^N \\ &\quad - T\,\frac{\mathcal{S}(\rho^N) - \mathcal{S}(\rho^{II})}{\rho^N} A^N, \end{aligned} \tag{24}$$

and we have used the definition of the volume fraction in each cell $f^N = V^N/V_W^N$. The single-nucleus free energy associated to the independent cell problem is given by the general

mean-field relation:

$$\tilde{F}_D(A^N) \equiv \frac{\partial \mathcal{F}}{\partial n_D} = F_D(A^N) + \delta F_D^N, \tag{25}$$

where δF_D^N is a rearrangement term. The rearrangement term arises from the self-consistency induced by the Coulomb term [27]. Indeed, the Coulomb term given by Eq. (14) explicitly depends on the local proton density ρ_p^N through the function Φ_D shown in Eq. (15). As the charge neutrality is realized at the level of the single Wigner-Seitz cell, its proton charge corresponding to the cluster N,

$$\rho_p = f^N\left(\rho_p^N - \rho_p^{II}\right) + \rho_p^{II}, \tag{26}$$

can be equalized to the global proton charge of the system given by Eq. (20). This equation can be written in terms of the cluster densities $n_D(A^N)$ as

$$\rho_p = \sum_{N,D} n_D(A^N) V^N\left(\rho_p^N - \rho_p^{II}\right) + \rho_p^{II}. \tag{27}$$

The equality between Eqs. (26) and (27) implies that the local proton density ρ_p^N depends on the probability of the associated fluctuation. As a consequence, a rearrangement term arises:

$$\delta F_D^N = \left(n_D \frac{\partial \tilde{F}_D}{\partial n_D}\right)(A^N). \tag{28}$$

Changing variables from ρ_p^N to the volume fraction f^N and using the virial relation $\mathcal{E}_{\mathrm{surf},D} = 2\mathcal{E}_{\mathrm{Coul},D}$ we have

$$\delta F_D^N = \frac{P_D(A^N)}{V_W} \frac{A^N V^N}{\rho^N} 3 \frac{\partial \mathcal{E}_{\mathrm{Coul},D}^N}{\partial f^N}. \tag{29}$$

As $\tilde{F}_D$ should scale with A^N, we factor out the A^N term, and average the rest of the expression over the different fluctuations, which amounts to replacing the different quantities with the ones obtained in the pasta calculation at the same thermodynamic conditions:

$$\delta F_D^N = A^N \frac{1}{\rho^I} 3 f \frac{\partial \mathcal{E}_{\mathrm{Coul},D}}{\partial f}, \tag{30}$$

which, after the replacement of Eq. (15), becomes

$$\delta F_D^N = \begin{cases} \frac{A^N}{\rho^I}\mathcal{E}_{\mathrm{Coul},3}\left(3 + \frac{1}{5\Phi_3}[f - f^{1/3}]\right), & \text{droplets} \\ \frac{A^N}{\rho^I}\mathcal{E}_{\mathrm{Coul},2}\left(3 + \frac{(f-1)}{4\Phi_2}\right), & \text{rods} \\ \frac{A^N}{\rho^I}\mathcal{E}_{\mathrm{Coul},1}\left(3 + \frac{1}{3\Phi_1}\frac{[f^2-1]}{f}\right), & \text{slabs} \end{cases}. \tag{31}$$

The calculation of the rearrangement term allows defining the total one-cell multicomponent free energy density as

$$\tilde{\mathcal{F}} = \sum_{N,D} n_D(A^N)\tilde{F}_D(A^N) + \mathcal{F}^{II}. \tag{32}$$

The grand-canonical partition sum of the independent cell problem can now be explicitly written as

$$\tilde{\mathcal{Z}} = \sum_{\{n_D\}} \exp -(\tilde{\mathcal{F}} - \mu_n\rho_n - \mu_p\rho_p)/T, \tag{33}$$

which can be factorized as

$$\tilde{\mathcal{Z}} = \tilde{\mathcal{Z}}_{\mathrm{clus}}\mathcal{Z}^{II}, \tag{34}$$

where $\mathcal{Z}^{II}$ is the partition sum of the homogeneous system at density ρ^{II}, $-T \ln \mathcal{Z}^{II} = \mathcal{F}^{II} - \sum_{q=p,n} \mu_q \rho_q^{II}$. Introducing the single-nucleus grand-canonical potential

$$\tilde{\Omega}_D(A^N) = \tilde{F}_D(A^N) - \mu^N \tag{35}$$

with the effective cluster chemical potential

$$\mu^N = \sum_{q=n,p} \mu_q V^N\left(\rho_q^N - \rho_q^{II}\right), \tag{36}$$

the clusterized part of the partition sum has the same functional structure as for an ideal gas, and can be explicitly calculated:

$$\begin{aligned} \tilde{\mathcal{Z}}_{\mathrm{clus}} &= \sum_{\{n_D\}} \exp -\left(\beta \sum_{N,D} n_D(A^N)\tilde{\Omega}_D(A^N)\right) \\ &= \prod_{N,D} \sum_{n=0}^{\infty} \frac{(\exp -\beta\tilde{\Omega}^N)^n}{n!} \\ &= \prod_{N,D} \exp w_D(A^N) \end{aligned} \tag{37}$$

with $w_D(A^N) = \exp -\beta\tilde{\Omega}_D(A^N)$ and $\beta = 1/T$. This leads to an analytical expression for the average cluster densities

$$n_D(A^N) = \frac{\partial \ln \tilde{\mathcal{Z}}_{\mathrm{clus}}}{\partial \beta \mu^N} = w_D(A^N), \tag{38}$$

and finally for the probabilities

$$P_D(A^N) = \frac{\exp(-\beta\tilde{\Omega}_D(A^N))}{\sum_D \sum_A \exp(-\beta\tilde{\Omega}_D(A))}, \tag{39}$$

such that the total probability of the fluctuation ρ^Ncan be calculated as $P^N = \sum_D P_D(A^N)$.

Equation (39) is our main result, and allows calculating the probability of the different pasta structures. We can see that we have formally recovered a simple Boltzmann weighting according to the different free energies of the clusters, biased

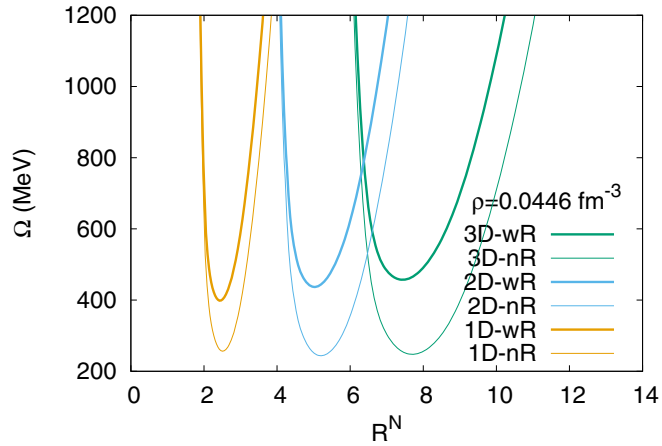

FIG. 2. Denser phase single-nucleus grand canonical potential with (wR, thick lines) and without (nR, thin lines) the rearrangement term for $T = 1$ MeV. 1D curves are on the left, 2D in the middle and 3D on the right.

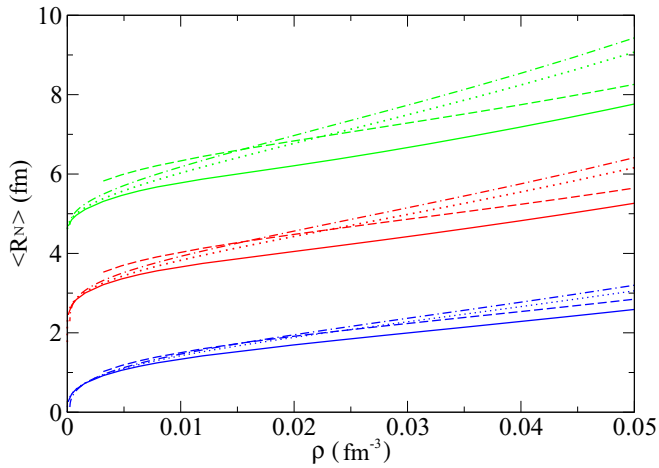

FIG. 3. Evolution with density of the linear size of the different geometries. Top curves stand for 3D, curves in the middle for 2D, and bottom curves for 1D. Solid lines represent $T = 1$ MeV and dashed lines $T = 4.5$ MeV for average distribution radius; dotted lines represent the pasta phase at 1 MeV and dot-dashed lines the pasta phase at $T = 4.5$ MeV.

by the chemical potentials that, for each thermodynamic condition, are taken from the SNA pasta calculation. However, the presence of the rearrangement term due to the Coulomb correlations imposed by charged neutrality modifies this simple picture. It was already shown in Refs. [27,38], where only spherical clusters were considered, that this term is essential to recover the SNA solution as the most probable cluster in the total multicomponent distribution. For this first application with the RMF model and the inclusion of the different pasta geometries, we limit ourselves to symmetric matter and neglect proton fraction fluctuations, i.e., we consider $Y_p^N = Y_p^I = Y_p^{II} = 0.5$. Then, the baryonic density in each cell is the same, $\rho_B^N = \rho_B$, and we simply have $f^N = \frac{\rho_B - \rho^{II}}{\rho^N - \rho^{II}}$.

To quantify the rearrangement term in the case of geometry fluctuations, we plot the Gibbs energy with (thick lines, higher values) and without (thin lines, lower values) it for the three lowest geometries at $T = 1$ MeV in Fig. 2. We can see that this term plays a non-negligible role and can even change the order of the preferential geometry.

III. RESULTS

To illustrate the formalism of Sec. II, we concentrate on the low density regime, close to the transition from the spherical to the rod shape, which is predicted by the NL3 model around $\rho_B = 0.03\,\mathrm{fm}^{-3}$ at zero temperature and at slightly different densities as the temperature increases.

Figure 3 displays the evolution with density of the average linear size of the different geometries for two different temperatures. We can see that the temperature effects are negligible, while bigger pasta structures appear in denser matter, as expected. This is in perfect agreement with the standard pasta calculation in the SNA (thin solid and dashed lines in Fig. 3), but in this latter a single geometry is considered in a given thermodynamic condition.

In our formalism, the different geometries can coexist and Fig. 4 shows the probability distribution as a function of the pasta linear dimension with different geometries and two temperatures, at two densities that correspond in the CPA approximation to the droplet and rod phase (see Fig. 1). We can see that the droplet configuration (3D) dominates at the lower density and both temperatures considered, but the contribution of the rod geometry is far from being negligible. At slightly higher density, the situation changes: the slab configuration (1D) dominates at both temperatures and the three geometries can be seen to coexist at $T = 5$ MeV. Whatever the geometry, the distribution is strongly peaked on the most probable cluster at the lowest temperature as expected, but considerable fluctuations are seen as the temperature increases.

The evolution with temperature of the probability of the different geometries is displayed in Fig. 5 for two different densities. The droplet geometry tends to prevail at the low temperature in the lower density regime considered and remains dominant at all temperatures. At the lower density, the slab configuration (1D) is hardly noticed. At the higher density, the spherical configuration is replaced by the slab one as the dominant geometry and the other two geometries (3D and 2D) are also present, as already observed in Fig. 4. Hence,

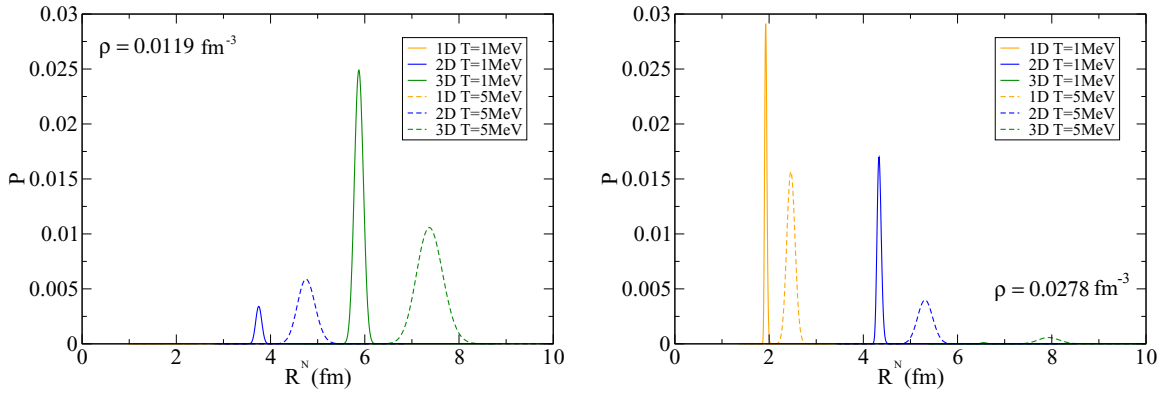

FIG. 4. Probability distribution as a function of the pasta linear dimension with different geometries, for different temperatures and densities with $Y_p = 0.5$. Solid lines represent $T = 1$ MeV and dashed lines $T = 5$ MeV.

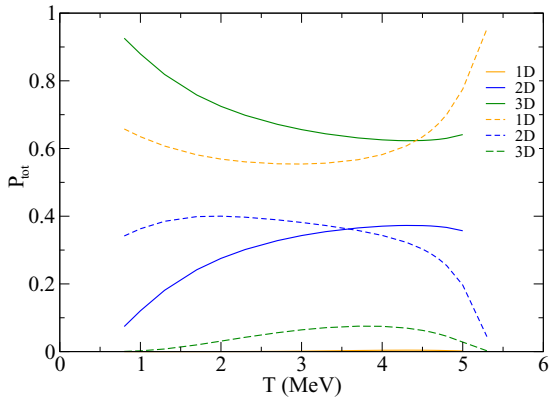

FIG. 5. Evolution with temperature of the probability of the different geometries. Solid lines represent $\rho = 0.0119$ fm^{-3} and dashed lines represents $\rho = 0.0278$ fm^{-3}. From top to bottom the solid curves stand for 3D, 2D, and 1D (hardly noticed) and the dashed curves for 1D, 2D, and 3D.

Fig. 5 demonstrates that in a very wide range of temperatures the geometries coexist with comparable probabilities.

IV. CONCLUSIONS

In this paper, we have extended a formalism recently introduced in Refs. [27,38] to the calculation of fluctuations of the pasta configurations. The statistical distribution of different pasta geometries and sizes is evaluated from the free energy functional of a single Wigner-Seitz cell, calculated with a relativistic mean field model with the coexisting phase approximation, and a surface tension fitted from Thomas-Fermi calculations at constant proton fraction. For this first application, we have restricted our efforts to symmetric matter and to a limited density region. We have shown that the droplets, rods, and slabs coexist with comparable probabilities in a large interval of densities and temperatures.

It is important to remark that in our formalism the pasta symmetry is always exactly respected. This is expected to be a good approximation at low temperature, well verified by microscopic calculations in three dimensions that allow all symmetry breakings [24]. However, more complicated geometries such as "waffle", "parking garage", and "TPMS" structures [21,25,26] are expected in some regimes of proton fractions, and could be added to the geometries presently considered. This might require extra corrections for applications in the supernova context where temperatures of the order of the MeV are explored. Indeed in this regime shape fluctuations are clearly observed in molecular dynamics simulations, even if finite thermalization time and finite size effects are difficult to handle and might distort the distributions [21,25].

Finally, it is important to recall that the presence of density inhomogeneities is known to contribute in an important way to neutrino opacity, and in general to the dynamics of supernova and neutron star cooling through a modification of the transport coefficients such as shear viscosity as well as electrical and thermal conductivities [10,13–15]. The evaluation of transport coefficients within our formalism is in progress, and will be presented in a forthcoming paper.

We would like to end by emphasizing the extremely low computational cost involved in our formalism as compared with [17,24–26] where the coexisting geometrical shapes are observed.

ACKNOWLEDGMENTS

This work was partially supported by Capes(Brazil)/ Cofecub (France) joint international collaboration Project No. 853/15 and is part of the project INCT-FNA Proc. No. 464898/2014-5. D.P.M. acknowledges partial support also from CNPq (Brazil) under Grant No. 301155/2017-8. D.P.M. and C.B. thank the LPC-Caen for the hospitality.

[1] H. T. Diep, *Magnetic Systems with Competing Interactions* (World Scientific, Singapore, 1994).
[2] D. G. Ravenhall, C. J. Pethick, and J. R. Wilson, Phys. Rev. Lett. **50**, 2066 (1983).
[3] M. Hashimoto, H. Seki, and M. Yamada, Prog. Theor. Phys. **71**, 320 (1984).
[4] C. J. Horowitz, M. A. Perez-Garcia, and J. Piekarewicz, Phys. Rev. C **69**, 045804 (2004).
[5] G. Watanabe, K. Sato, K. Yasuoka, and T. Ebisuzaki, Phys. Rev. C **66**, 012801(R) (2002).
[6] T. Maruyama, T. Tatsumi, D. N. Voskresensky, T. Tanigawa, and S. Chiba, Phys. Rev. C **72**, 015802 (2005).
[7] E. F. Brown and A. Cumming, Astrophys. J. **698**, 1020 (2009).
[8] A. Deibel, A. Cumming, E. F. Brown, and S. Reddy, Astrophys. J. **839**, 95 (2017).
[9] J. A. Pons, D. Vigan, and N. Rea, Nat. Phys. **9**, 431 (2013).
[10] C. J. Horowitz, D. K. Berry, C. M. Briggs, M. E. Caplan, A. Cumming, and A. S. Schneider, Phys. Rev. Lett. **114**, 031102 (2015).
[11] H. Sotani, Mon. Not. R. Astron. Soc. **417**, L70 (2011).
[12] C. J. Horowitz, Phys. Rev. D **81**, 103001 (2010).
[13] M. D. Alloy and D. P. Menezes, Phys. Rev. C **83**, 035803 (2011).
[14] U. J. Furtado, S. S. Avancini, J. R. Marinelli, W. Martarello, and C. Providencia, Eur. Phys. J. A **52**, 290 (2016).
[15] R. Nandi and S. Schramm, Astrophys. J. **852**, 135 (2018).
[16] C. J. Horowitz, D. K. Berry, M. E. Caplan, T. Fischer, Z. Lin, W. G. Newton, E. O'Connor, and L. F. Roberts, arXiv:1611.10226 [astro-ph.HE] (2016).
[17] A. S. Schneider, D. K. Berry, M. E. Caplan, C. J. Horowitz, and Z. Lin, Phys. Rev. C **93**, 065806 (2016).
[18] S. Kubis and W. Wójcik, The Eur. Phys. J. A **54**, 215 (2018).
[19] J. Daligault and S. Gupta, Astrophys. J. **703**, 994 (2009).
[20] P. N. Alcain and C. O. Dorso, Phys. Rev. C **97**, 015803 (2018).
[21] A. S. Schneider, M. E. Caplan, D. K. Berry, and C. J. Horowitz, Phys. Rev. C **98**, 055801 (2018).
[22] W. G. Newton and J. R. Stone, Phys. Rev. C **79**, 055801 (2009).

[23] F. Sebille, V. de la Mota, and S. Figerou, Phys. Rev. C **84**, 055801 (2011).
[24] M. Okamoto, T. Maruyama, K. Yabana, and T. Tatsumi, Phys. Rev. C **88**, 025801 (2013).
[25] F. J. Fattoyev, C. J. Horowitz, and B. Schuetrumpf, Phys. Rev. C **95**, 055804 (2017).
[26] B. Schuetrumpf, G. Martínez-Pinedo, Md. Afibuzzaman, and H. M. Aktulga, Phys. Rev. C **100**, 045806 (2019).
[27] G. Grams, S. Giraud, A. F. Fantina, and F. Gulminelli, Phys. Rev. C **97**, 035807 (2018).
[28] A. Burrows and J. M. Lattimer, Astrophys. J. **285**, 294 (1984).
[29] G. A. Lalazissis, J. König, and P. Ring, Phys. Rev. C **55**, 540 (1997).
[30] M. Dutra, O. Lourenço, S. S. Avancini, B. V. Carlson, A. Delfino, D. P. Menezes, C. Providência, S. Typel, and J. R. Stone, Phys. Rev. C **90**, 055203 (2014).
[31] S. S. Avancini, C. C. Barros, Jr., L. Brito, S. Chiacchiera, D. P. Menezes, and C. Providência, Phys. Rev. C **85**, 035806 (2012).
[32] S. S. Avancini, L. Brito, J. R. Marinelli, D. P. Menezes, M. M. W. de Moraes, C. Providência, and A. M. Santos, Phys. Rev. C **79**, 035804 (2009).
[33] S. S. Avancini, D. P. Menezes, M. D. Alloy, J. R. Marinelli, M. M. W. Moraes, and C. Providência, Phys. Rev. C **78**, 015802 (2008).
[34] H. Shen, H. Toki, K. Oyamatsu, and K. Sumiyoshi, Nucl. Phys. A **637**, 435 (1998).
[35] S. S. Avancini, C. C. Barros, Jr., D. P. Menezes, and C. Providência, Phys. Rev. C **82**, 025808 (2010).
[36] C. Providencia, S. S. Avancini, R. Cavagnoli, S. Chiacchiera, C. Ducoin, F. Grill, J. Margueron, D. P. Menezes, A. Rabhi, and I. Vidana, Eur. Phys. J. A **50**, 44 (2014).
[37] F. Gulminelli and Ad. R. Raduta, Phys. Rev. C **92**, 055803 (2015).
[38] A. F. Fantina, S. De Ridder, N. Chamel, and F. Gulminelli, Astron. Astrophys. **633**, A149 (2020).